



HAL
open science

Measurement of the quantum geometric tensor and of the anomalous Hall drift

A. Gianfrate, O. Bleu, L. Dominici, V. Ardizzone, M. de Giorgi, D. Ballarini, G. Lerario, K. West, L. N Pfeiffer, D. Solnyshkov, et al.

► **To cite this version:**

A. Gianfrate, O. Bleu, L. Dominici, V. Ardizzone, M. de Giorgi, et al.. Measurement of the quantum geometric tensor and of the anomalous Hall drift. *Nature*, 2020, 578 (7795), pp.381-385. 10.1038/s41586-020-1989-2 . hal-03040760

HAL Id: hal-03040760

<https://hal.science/hal-03040760>

Submitted on 4 Dec 2020

HAL is a multi-disciplinary open access archive for the deposit and dissemination of scientific research documents, whether they are published or not. The documents may come from teaching and research institutions in France or abroad, or from public or private research centers.

L'archive ouverte pluridisciplinaire **HAL**, est destinée au dépôt et à la diffusion de documents scientifiques de niveau recherche, publiés ou non, émanant des établissements d'enseignement et de recherche français ou étrangers, des laboratoires publics ou privés.

Direct measurement of the quantum geometric tensor and of the anomalous Hall drift in a two-dimensional continuous medium

A. Gianfrate¹, O. Bleu^{2*}, L. Dominici¹, V. Ardizzone¹, M. De Giorgi¹, D. Ballarini¹, G. Lerario¹, K. West³, L. N. Pfeiffer³, D. D. Solnyshkov², D. Sanvitto¹, G. Malpuech²

¹*CNR NANOTEC, Istituto di Nanotecnologia, via Monteroni, 73100 Lecce, Italy.*

²*Institut Pascal, PHOTON-N2, Université Clermont Auvergne, CNRS, SIGMA Clermont, F-63000 Clermont-Ferrand, France.*

³*PRISM, Princeton Institute for the Science and Technology of Materials, Princeton University, Princeton, New Jersey 08540, USA*

Topological Physics relies on the specific structure of the eigenstates of Hamiltonians. Their geometry is encoded in the quantum geometric tensor ¹ containing both the celebrated Berry curvature ², crucial for topological matter ³, and the quantum metric ⁴. The latter is at the heart of a growing number of physical phenomena such as superfluidity in flat bands ⁵, orbital magnetic susceptibility ^{6,7}, exciton Lamb shift ⁸, and non-adiabatic corrections to the anomalous Hall effect ^{6,9}. Here, we report the first direct measurement of both Berry curvature and quantum metric in a two-dimensional continuous medium, together with the related anomalous Hall drift of an accelerated wavepacket. The studied platform is a planar microcavity of extremely high finesse, in the strong coupling regime ¹⁰. It hosts mixed exciton-photon modes (exciton-polaritons) subject to photonic spin-orbit-coupling ¹¹, which

*These authors contributed equally: A. Gianfrate, O. Bleu

makes emerge Dirac cones ¹², and to exciton Zeeman splitting, breaking time-reversal symmetry. The monopolar and half-skyrmion pseudospin textures are measured by polarisation-resolved photoluminescence. The associated quantum geometry of the bands is extracted and allows to predict the anomalous Hall drift, which we independently measure using high resolution spatially-resolved epifluorescence. Our results unveil the intrinsic chirality of photonic modes which is the cornerstone of topological photonics ¹³⁻¹⁵. They validate experimentally the semiclassical description of wave packet motion in geometrically non-trivial bands ^{9,16}. The use of exciton-polaritons (interacting photons) opens wide perspectives for future studies of quantum fluid physics in topological systems.

One of the striking manifestations of topological effects in Physics is the conductance quantization in the two-dimensional (2D) quantum Hall effect (QHE). This perfect quantization relies on a topological invariant characterising the global band properties: the Chern number. Non-zero Chern numbers are associated with the chiral conducting edge states in topological insulators and superconductors ³. Beyond electronic systems, topological band concepts have been extended to a variety of wave systems covering photonics ^{14,15}, acoustics ¹⁷, cold atoms ¹⁸, and even geophysics ¹⁹.

Topological effects are not encoded in the energy spectrum of the system but rely on the non-trivial geometry of the eigenstates. It is the gauge invariant quantum geometric tensor (QGT) that contains the structural information about the eigenstates of a parametrised Hamiltonian. The QGT has a symmetric real part which defines the quantum metric characterising distances between

states ⁴ in a parameter space. Its antisymmetric imaginary part determines the Berry curvature ² whose momentum space distribution is crucial in modern Physics. Locally, it is responsible for the anomalous Hall transport ¹⁶ in the intrinsic spin Hall and valley Hall effects. Its integral over a 2D closed manifold gives the Chern number. On the other hand, the quantum metric, related to the concept of fidelity in quantum information theory, also describes important physical phenomena. It can probe quantum phase transitions when defined in an arbitrary parameter space ²⁰. The *momentum* space metric affects the electronic orbital magnetic susceptibility ^{6,7} in crystals and the exciton Lamb shift in Transitional Metal Dichalcogenides ⁸. It characterises superfluidity and bogolon current in flat bands ^{5,21} and also corrections to the semiclassical equations describing the anomalous Hall effect ^{6,9}.

The extension of topological concepts from solid state physics to other classical or quantum systems has opened new possibilities for measuring local geometrical properties of bands, and not only the global ones (like the conductivity in QHE). Several protocols have been proposed to measure the Berry curvature ^{22,23}. Experimental reconstructions via indirect dynamical measurements have been reported ^{24,25}. The parameter space geometry of two-level systems has been explored experimentally even more recently ^{26,27}. In this work, we present a direct measurement of the full momentum space QGT (Berry curvature and quantum metric) of the 2D bands of a homogeneous system. Furthermore, we measure independently the dynamics of an accelerated wavepacket which demonstrates anomalous Hall drift. This drift is reproduced by semiclassical equation of motion ^{9,16} including the measured band geometry as an input parameter.

Our experimental platform is a high-quality planar microcavity ($Q > 10^5$) with embedded quantum wells supporting 2D strongly coupled exciton-photon bands (Supplementary Figure 6)¹⁰. Each band is doubly polarisation degenerate and forms a pseudo-spinor. The polarisation degeneracy is lifted by the photonic splitting between TE and TM (Transverse-Electric and Transverse-Magnetic) eigenmodes¹¹ and, under magnetic field, by the exciton Zeeman splitting. The polarised polariton eigenstates are exactly determined by a Fourier space mapping of polarisation-resolved photoluminescence (PL). They exhibit non-zero Berry curvature and quantum metric as discussed below.

Before presenting the measurements, let us remind the properties of an effective two-band Hamiltonian²⁸ describing, in the conservative limit, the lower polariton branch in the circular polarisation basis¹⁰:

$$H_{\mathbf{k}} = \begin{pmatrix} \frac{\hbar^2 k^2}{2m^*} + \Delta_z & \alpha - \beta k^2 e^{-2i\varphi} \\ \alpha - \beta k^2 e^{2i\varphi} & \frac{\hbar^2 k^2}{2m^*} - \Delta_z \end{pmatrix} \quad (1)$$

where $m^* = m_l m_t / (m_l + m_t)$, with m_l and m_t being the longitudinal and transverse effective masses. $k = |\mathbf{k}| = \sqrt{k_H^2 + k_V^2}$ is the in-plane wavevector ($k_H = k \cos \varphi$, $k_V = k \sin \varphi$, φ is the propagation angle). Δ_z is the polariton Zeeman splitting (due to the excitonic part). α is the optical birefringence, unavoidable in crystalline systems. It leads to a k -independent splitting between horizontally and vertically (HV) polarised states. β quantifies the k -dependent TE-TM splitting, ubiquitous in 2D photonic systems, which makes 2D photonic bands geometrically non-trivial. This 2×2 Hamiltonian can be decomposed in Pauli matrices, describing the interaction

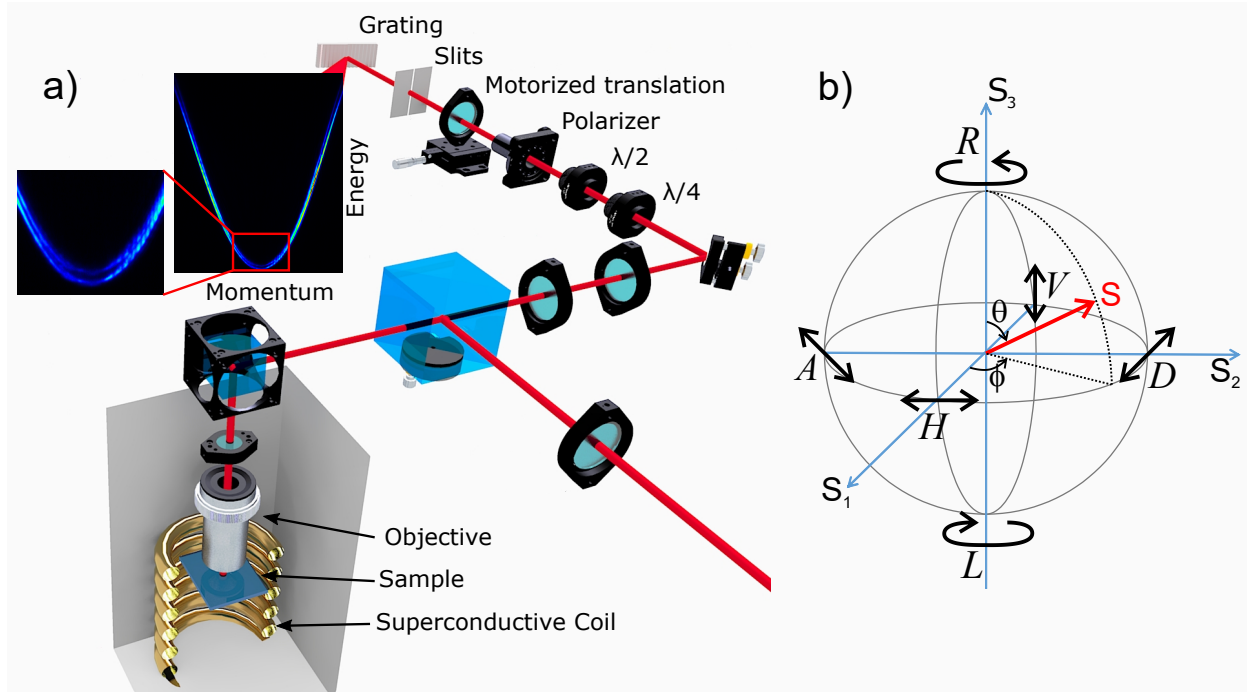


Figure 1: **Experimental setup and the Poincaré sphere** a) Scheme of the polarisation tomography experiment. The incoming pump laser (bottom right) is focused onto the sample held in the cryogenic superconductive magnet (bottom left). The emission is recollimated, polarisation filtered and the momentum space optically rebuilt at the entrance slits of a spectrometer (top) with energy resolution (top left). The Zeeman splitting is highlighted in the inset. b) Pseudospin (Stokes vector) orientation on the Poincaré sphere parametrised by the angles θ and ϕ . The pseudospin coordinates S_1, S_2, S_3 are measured through the polarisation degree of emission of one state on the Horizontal/Vertical (HV), Diagonal/Anti-diagonal (DA), and circular Right/Left (RL) polarisation basis [Eq. (5)].

between an effective magnetic field and a pseudospin:

$$H_{\mathbf{k}} = \frac{\hbar^2 k^2}{2m^*} \mathbb{I} + \mathbf{\Omega}(\mathbf{k}) \cdot \boldsymbol{\sigma} \quad (2)$$

$\mathbf{S} = \langle \sigma \rangle$ is here the polarisation pseudospin of light. The effective field reads:

$$\mathbf{\Omega}(\mathbf{k}) = \begin{pmatrix} \alpha - \beta k^2 \cos 2\varphi \\ -\beta k^2 \sin 2\varphi \\ \Delta_z \end{pmatrix} \quad (3)$$

Eigenstates have their pseudospin parallel and anti-parallel with the effective field. The QGT components are linked with the variation of the pseudospin orientation in k -space as²⁸:

$$\begin{aligned} g_{ij} &= \frac{1}{4} (\partial_{k_i} \theta \partial_{k_j} \theta + \sin^2 \theta \partial_{k_i} \phi \partial_{k_j} \phi) \\ B_z &= \frac{1}{2} \sin \theta (\partial_{k_i} \theta \partial_{k_j} \phi - \partial_{k_j} \theta \partial_{k_i} \phi) \end{aligned} \quad (4)$$

with g_{ij} the metric components and B_z the Berry curvature, which cancels if the TE-TM spin-orbit coupling vanishes ($\beta = 0$). $\theta(\mathbf{k})$ and $\phi(\mathbf{k})$ are polar and azimuthal angles parametrising the eigenstate $\psi = (\cos \frac{\theta}{2} e^{-i\phi}, \sin \frac{\theta}{2})^T$ and the pseudospin position on the Poincaré sphere [Fig. 1(b)] with $\theta = \arccos S_3$ and $\phi = \arctan S_2/S_1$. These quantities are computed analytically²⁸ from the eigenstates of (1) (Supplementary Note 1).

The sample studied is a high-quality microcavity with a 100 ps lifetime (Methods). The experimental setup is shown in Fig. 1(a). The measurements are executed at 4K in a reflection configuration under an applied external magnetic field. We first use off-resonant continuous wave laser excitation. PL is measured versus the 2D wavevector and energy for all 6 polarisation axes of the Poincaré sphere (Fig. 1(b)). For each wavevector, the energies of the polarization doublet are

found by Gaussian fitting of the emission. Their pseudospin is determined from the polarisation intensities as:

$$S_1(\mathbf{k}) = \frac{I_H - I_V}{I_H + I_V}, \quad S_2(\mathbf{k}) = \frac{I_D - I_A}{I_D + I_A}, \quad S_3(\mathbf{k}) = \frac{I_R - I_L}{I_R + I_L} \quad (5)$$

The k-space pseudospin distribution then allows to compute the QGT components of each branch using Eq. (4).

Figure 2 shows the 0 T measurements (no Zeeman splitting, $\Delta_z = 0$) at zero exciton-photon detuning (Methods). The energy dispersion extracted from the raw PL (Methods, Supplementary Note 2) is shown in Fig. 2(a) (inset shows the energy difference). By fitting the dispersion, we obtain the polariton mass $m = (9.2 \pm 0.1) \times 10^{-5} m_0$ (m_0 is the free electron mass), the TE-TM splitting $2\beta = 26.3 \pm 0.3 \mu\text{eV}\mu\text{m}^2$, and the birefringence (HV-splitting) $2\alpha = 15.3 \pm 0.6 \mu\text{eV}$ at $k = 0$. If this HV splitting were zero ($\alpha = 0$), the dispersion would be composed of two parabola of different masses touching at $k = 0$, similar to the quadratic band degeneracies in bilayer graphene. The Berry phase accumulated along a closed loop around the band touching point would be 2π (Berry topological charge 1). When the HV-splitting is non-zero ($\alpha \neq 0$), as in our sample, the cylindrical symmetry is broken. Along k_H , the lowest energy mode has the smallest mass. The two parabola cross at $k_0 = \sqrt{\alpha/\beta} \approx 0.8 \mu\text{m}^{-1}$ where the TE-TM and HV- splitting compensate. Along k_V such points are absent, since both contributions add up. This is visible in Fig. 2(b,c), showing the HV and DA polarisation degree of the lower band (the circular polarisation degree is zero at 0 T).

The degeneracy points, marked by crosses, are tilted Dirac cones, around which the effective

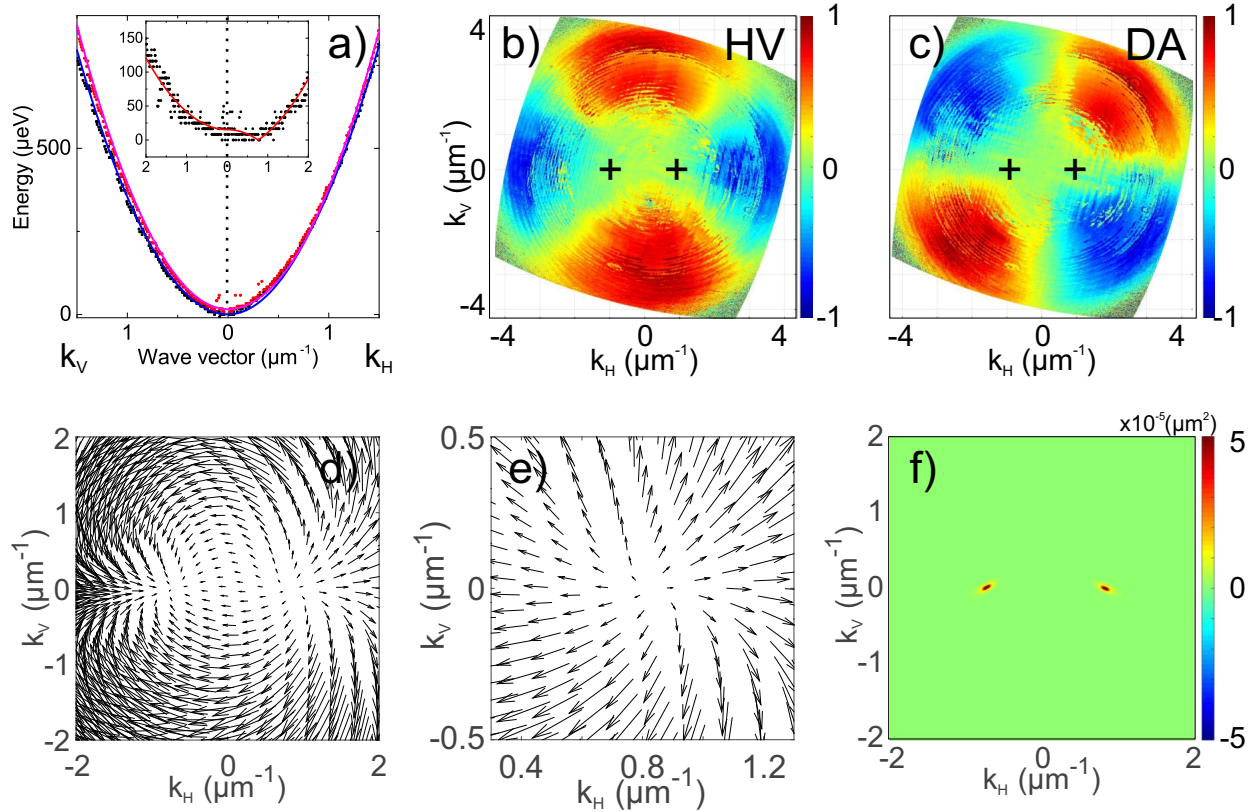


Figure 2: **Emergence of pseudospin monopoles.** Data from PL at 0 T. a) The two eigenmode energies along the two orthogonal momentum directions k_H and k_V . The zero is at ~ 1600 meV (bottom of the polariton branch). Inset: eigenmodes energy splitting. Points - experimental data. Solid lines - fit with Eq. (1). (b,c) HV and DA polarisation degree maps of the lower mode in the full 2D momentum space. The crosses mark the degeneracy points. (d,e) The corresponding in-plane pseudospin (S_1, S_2) texture distribution in k -space, shown on a wide scale (d), and zoomed on one of the crossing points (e), demonstrating a monopole pseudospin texture. (f) k -space distribution of the trace of the quantum metric tensor ($g_{HH} + g_{VV}$), peaked around the two monopoles.

field and pseudospin textures look like 2D monopoles [Fig. 2(d,e)]. The breaking of the TE-TM rotational symmetry by the HV field induces the separation of the TE-TM vector field of winding number 2 into a pair of 2D monopoles of winding 1, but of opposite divergences. Each monopole carries a Berry topological charge $1/2$, so that the band topology does not depend on the HV-splitting, but the band geometry does. The Berry curvature of each monopole is a delta function, whereas the metric has a finite extension measured in Fig. 2(f). Therefore, any finite-duration measurement of the Berry phase performed making a loop around these points should show a deviation from the adiabatic value of π quantified by this metric distribution. These effective monopoles can be mapped to emergent non-Abelian gauge fields acting on photons¹². Interestingly, the metric distribution around the crossing points is not cylindrically symmetric, which might be due to non-hermiticity²⁹.

Now we break the time-reversal symmetry, applying a 9 T magnetic field described by the Zeeman term Δ_z . The field also makes the exciton-photon detuning slightly negative (Methods) because of the exciton diamagnetic shift. Panel 3(a) shows the dispersions along k_H and k_V , as in Fig. 2(a) (inset shows the energy difference). The modes are now split everywhere in k -space and at $k = 0$ the energy splitting is $\approx 102 \mu\text{eV}$. The crossing along k_H becomes an anticrossing. The splitting at the anti-crossing point is the polariton Zeeman splitting $2\Delta_z = 100.9 \pm 0.6 \mu\text{eV}$ caused by the excitonic part (exciton g-factor ~ 0.2). It is ten times larger than the linewidth of our ultra-high quality sample which is quite significant, despite the optical frequency operation. The measured polarisation degrees are shown in Figs. 3(b-d). The polarisation at $k = 0$ becomes elliptical. The circular polarisation degree decreases along k_V and increases along k_H up to $\pm k_0$,

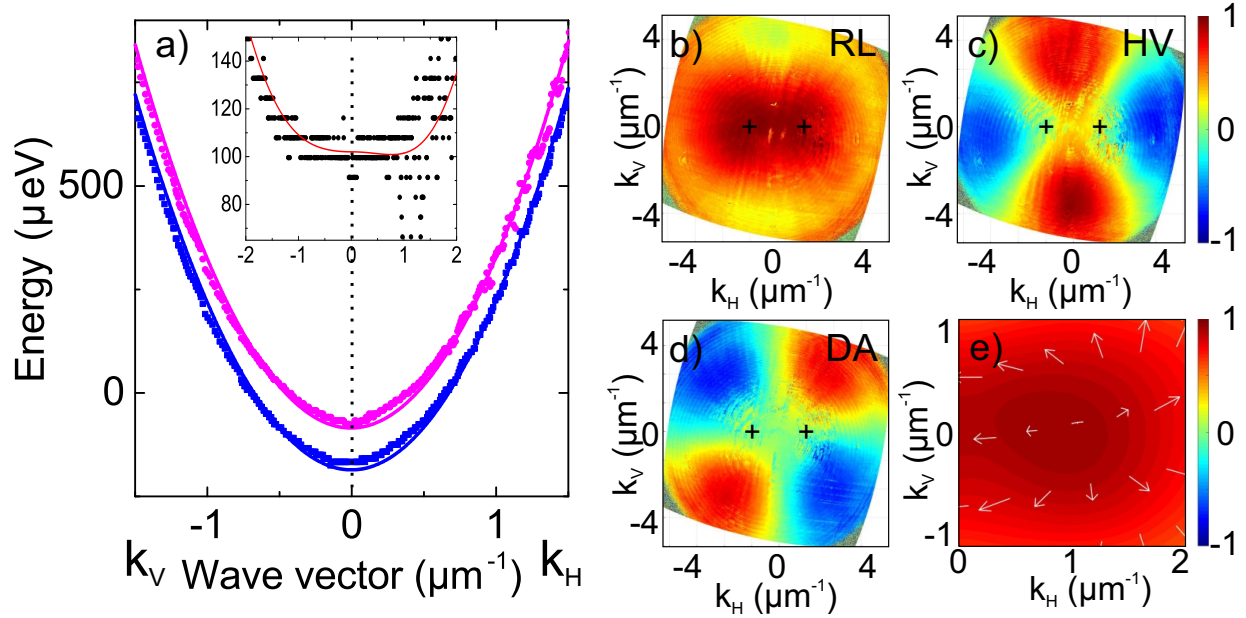


Figure 3: **Broken time-reversal symmetry: Emergence of half-skyrmion pseudospin textures.**

Data from PL at 9T. a) Energy dispersion along k_H and k_V . Anticrossing of the branches is observed instead of their crossing. The polarisation bands are split for all wave-vectors (see inset, where along k_V , the splitting has a non-zero minimum). (b,c,d) RL, HV, and DA polarisation degree maps of the lower energy mode. The crosses mark the anti-crossing points. e) Pseudospin distribution in k -space, zoomed near one of the crossing points. The in-plane pseudospin (S_1, S_2) is shown by the white arrows, S_3 amplitude is shown by colour.

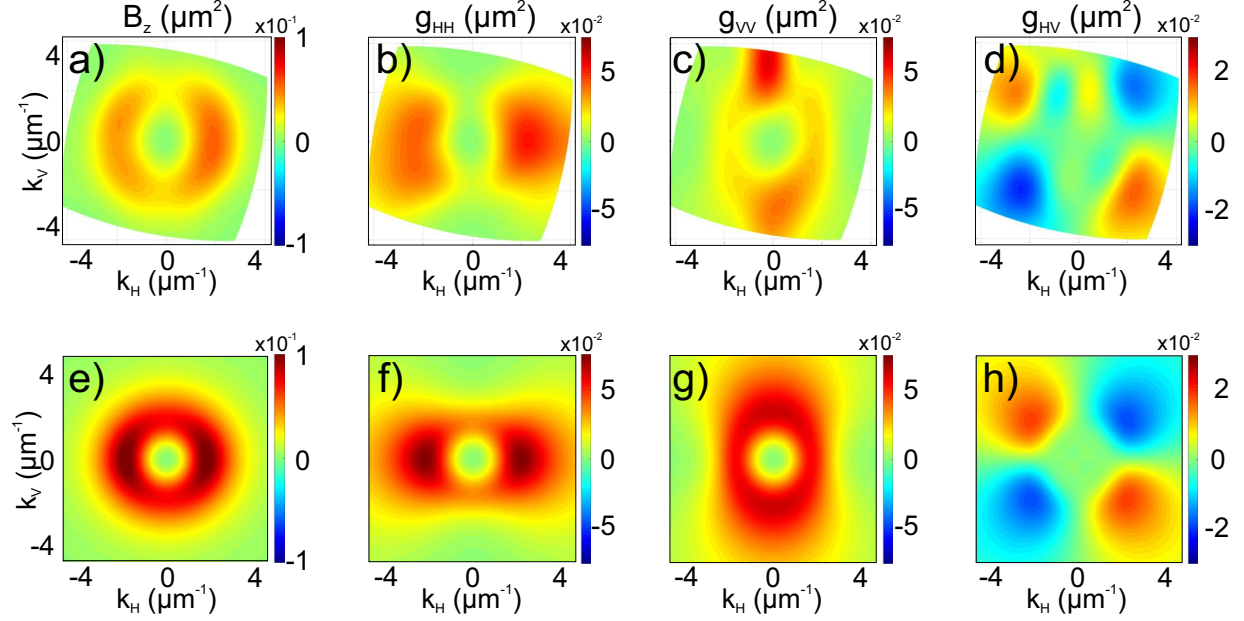


Figure 4: **Berry curvature and quantum metric distributions.** (a-d) - experiment (PL at 9 T). k -space distribution of QGT elements: (a) Berry curvature B_z , (b) g_{HH} , (c) g_{VV} , (d) g_{HV} , extracted using Eq. (4). (e-h) - theory. The computation is based on the effective Hamiltonian (1) and Supplementary Note 1.

where it becomes close to 1. A zoom on the measured pseudospin texture around k_0 is shown in Fig. 3(e), exhibiting a part of a half-skyrmion, as expected.

The k -space distributions of the Berry curvature and of the three components of the quantum metric tensor, extracted from the experimental data of Fig. 3 using Eq. (4), are shown in Figs. 4(a-d). They are compared with analytical calculations [Figs. 4(e-h), Supplementary Note 1] performed using the parameters extracted from the dispersions in Fig. 2(a), 3(a). Without HV-splitting, the Berry curvature would be circularly symmetric, whereas for a dominating HV-splitting the distribution would be concentrated around the anti-crossing points. Here, we are between these two

limiting cases. A similar procedure applied to the second polarisation branch (Supplementary Figure 4) confirms that the two branches are cross-polarised, show opposite Berry curvatures and the same quantum metric elements.

A consequence of non-trivial band geometry is the anomalous Hall drift of an accelerated wavepacket which appears as a correction in the semiclassical equation of motion ¹⁶:

$$\hbar \frac{\partial \mathbf{r}}{\partial t} = \frac{\partial E}{\partial \mathbf{k}} + \mathbf{F} \times \mathbf{B} \quad (6)$$

where \mathbf{r} is the wavepacket center of mass, $E(\mathbf{k})$ is the dispersion, $\mathbf{F}(\mathbf{k})$ is the accelerating force, $\mathbf{B} = B_z \mathbf{e}_z$. The acceleration is provided by the thickness gradient of the microcavity. The resulting energy gradient accelerates polaritons like an electric field accelerates charges. We choose a sample region with the largest gradients of 6 meV/mm and negative exciton-photon detuning. The gradient is measured independently (Supplementary Note 3) and exhibits a slight spatial variation (saddle-type potential). We selectively excite the lower polariton branch at $k = 0$ with a *cw* laser (30 μm size spot). Fig. 5(a) shows the spatial distribution of the intensity at ± 9 T (removing noise) under elliptically-polarised excitation of the lower eigenstate (Methods). The two traces separate along their propagation. This is confirmed in Fig. 5(b), showing the measured centre-of-mass trajectories, well reproduced by numerical simulations based on the semiclassical equation (6), using as input parameters the potential and the Berry curvature distribution computed using (1),(4) and the experimentally fitted parameters. Interestingly, this saddle-like potential magnifies the drift by a factor 1.6 with respect to a constant gradient (Supplementary Note 3). The oscillations of experimental trajectories are attributed to sample disorder. They remain smaller than the significant global drift. The role of non-adiabaticity on the trajectories, quantified by the quantum metric ⁹,

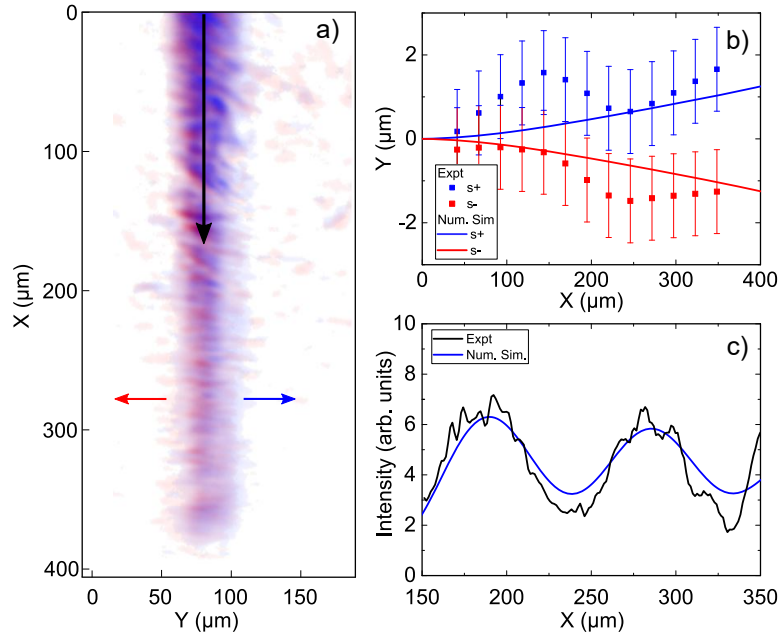


Figure 5: **Polariton anomalous Hall effect.** cw resonant excitation of the lower polariton mode at $k = 0$ with $30 \mu\text{m}$ size excitation spot. For (a) and (b) the polarisation is elliptical corresponding to the polarisation of the eigenstate. (a) Spatial distribution of emission at +9 T (pink) and -9 T (blue). (b) Center of mass trajectory at +9 T and -9 T respectively. The experiment is shown by squares with error bars and theory based on the semiclassical equation by solid lines. (c) The polarisation of excitation is circular which leads to oscillations of the intensity of emission in the cross-circular polarisation (black – experiment, blue – theory).

cannot be evidenced here considering the experimental uncertainties. However, non-adiabaticity can be increased by modifying the excitation conditions. Fig. 5(c) shows the cross-polarised emission when the excitation is circularly polarised, slightly exciting the upper polarisation eigenstate (black – experiment, blue – full Schrödinger simulation, Supplementary Note 3). The contrast of these oscillations is the non-adiabatic fraction, also given by the distance between the quantum states at $k = 0$ and $k = k_0$ determined from the metric g_{ij} (Supplementary Note 4) as:

$$|f_1|^2 \approx \left(\int_{|\psi_0(0)\rangle}^{|\psi_0(k_0)\rangle} \sqrt{\sum_{ij} g_{ij} \frac{dk^i}{dt} \frac{dk^j}{dt}} dt \right)^2 \quad (7)$$

where dt is taken along the shortest distance path. The distance that we estimate from the oscillations is 0.16 ± 0.02 , while the expression (7) gives 0.18 ± 0.03 , showing a remarkable agreement.

Our experiments provide a measure of both the full non-trivial band geometry of a 2D continuous system and, independently, real space wavepacket motion demonstrating anomalous Hall effect and non-adiabaticity. It supports the validity of the semiclassical approach and band geometry to compute wavepacket dynamics. Our results demonstrate that 2D photonic modes, because they are TE and TM polarised, carry topological charges, essential for topological photonics. Indeed, by using an appropriate lattice, the geometrically non-trivial bulk photon dispersion transforms into gapped topologically non-trivial photonic Bloch bands^{13–15,30,31} whose QGT can be explored by our technique²⁸. The polaritonic platform (interacting photons) able to demonstrate lasing and quantum fluid behaviour (superfluidity, quantized vortices...) opens wide perspectives for topological physics. It already brought striking breakthroughs, such as topological lasers³², and offers exciting possibilities, such as mixing different topological effects related to quantum vortices and

band structures³³.

Methods

Sample details. The sample used for this experiment is a high quality-factor $3/2 \lambda$ GaAs/AlGaAs planar cavity. The advanced control of molecular beam epitaxy (MBE) of the grower results in a quality factor widely exceeding 100.000, the associated lifetime τ for the lower polariton branch surpass 100 ps. This lifetime is measured making propagation experiments at negative exciton-photon detuning, as done in^{34,35}. Moreover, the quantum wells show large areas (up to several hundreds of μm) free from defects. The cavity contains 12 GaAs quantum wells, 7 nm thick, organised in groups of 4 placed at three anti-node positions of the electric field. The front (back) mirror consists of 34 (40) pairs of AlAs/Al_{0.80}Ga_{0.20}As layers. The exciton energy is $E_{exc} = 1.611$ eV and the Rabi splitting is $\hbar\Omega_R \approx 16$ meV at 0 T. The full polariton dispersion measurement evidencing the exciton-photon anticrossing is shown in the Supplementary Figure 6.

The exciton diamagnetic shift (red shift) is 4 meV at 9 T. The oscillator strength increases when applying 9 T, leading to a 17% increment of the Rabi splitting. These two effects almost compensate each other, resulting in a small blueshift of the bottom of the lower polariton branch of 0.4 meV at 9 T. The exciton-photon detuning (see below) is therefore more negative by 4 meV at 9 T with respect to 0 T. This detuning change remains relatively moderate compared with the Rabi splitting value. The exciton fraction of the exciton-polariton is reduced from 0.5 at 0 T to about 0.4 at 9 T while the photon fraction increases from 0.5 to about 0.6. The exciton diamagnetic shift and the increase of the exciton oscillator strength are well-known effects due to the decrease of the

exciton Bohr radius under magnetic field ^{36,37}.

Exciton-photon detuning. One of the most important parameters controlling the properties of exciton-polaritons is the exciton-photon detuning ¹⁰, which is the difference between the energies of the two bare resonances at $k = 0$: $\delta = E_{phot} - E_{exc}$. This parameter controls the excitonic and photonic fractions of the lower polariton branch, or rather their deviation from the equal values of 50% at $\delta = 0$. For example, the excitonic fraction (square of the Hopfield coefficient) for relatively small detunings reads: $x(\delta) \approx 1/2 + \delta/2\hbar\Omega_R$. As an example, going towards negative detuning makes polaritons more photonic, which means (among other things) that the exciton-related Zeeman splitting Δ_z decreases, while the photon-related spin-orbit coupling β increases.

In order to perform the two experiments, the QGT and the Anomalous Hall Drift (AHD) measures shown in the main text, we selected two different regions of the same wafer. For the QGT measure, we selected a central region of the sample at $\delta = 0$ meV at 0T. On the other hand, in order to have the adiabatic acceleration needed to observe the AHD effect, we selected a lateral region of the same wafer showing a rapid change in the energy of the lower polariton branch, (≈ 3 nm/mm), and a negative detuning of $\delta \approx -10$ meV.

Experimental setup to measure the QGT. The microcavity is cooled to 4 K in a closed loop helium cryostat equipped with a superconductive magnet able to generate a field onto the sample that spans from -9 to 9 T in a Faraday configuration (external magnetic field perpendicular to the microcavity plane).

For the measurement of the QGT, the excitation is performed by an off-resonant linearly po-

larized continuous wave $2 \mu\text{m}$ laser spot, tuned to the first minimum of the stopband oscillations in order to maximize the injection. The sample excitation and polaritonic PL collection is performed in a reflection scheme, by means of a wide numerical aperture objective (0.86), resulting in a $14 \mu\text{m}^{-1}$ field of view. A $8 \mu\text{m}^{-1}$ portion of k space is then reconstructed on the monochromator slits so that the PL can be energetically resolved. In order to avoid any loss of information of k space, the entire detection line is built in a 2f configuration and the needed polarisation filtering is performed in the real space plane. The polarisation response of the setup is characterised prior to the experiments. The raw PL data are collected by an automatised Labview routine able to perform a complete tomography in any of the 3 polarisation bases (H/V, A/D, and R/L), via the sequential passage of light through a couple of motorised quarter- and half-waveplates and a polariser. The energy mapping onto the charge-coupled device (CCD) camera is performed throughout a 550 cm monochromator equipped with a 1800 lines/mm grating and slits aperture set to $80 \mu\text{m}$. For each polarisation, a scan of 561 images is acquired, each containing a $I(E, k_V)$ map at a given k_H , upon moving a translational stage mounting the final lens by steps of $12 \mu\text{m}$. In this way, a 3D set of PL data $[I(E, k_H, k_V)]$ is collected in any of the 6 polarisation states. The image energy resolution is $\delta E = 0.015 \text{ nm}$. The momentum resolution are $\delta k_V = 0.008 \mu\text{m}^{-1} \cdot \text{pixel}^{-1}$ and $\delta k_H = 0.014 \mu\text{m}^{-1} \cdot \text{frame}^{-1}$, corresponding to the momentum magnification with respect to the CCD pixel size and scan lens movement step, respectively.

Experimental setup to measure polariton anomalous Hall effect. The anomalous Hall drift experiment is also performed in reflection configuration, in the same cryostat at the same temperature and magnetic field conditions, but using a 3 cm focal distance doublet ensuring a real

space field of view exceeding $500 \mu\text{m}$. Resonant excitation of the lower polariton mode at $k = 0$ is performed, with a polarisation of excitation which is adjusted to the one of the eigenstates. The chosen region of the sample exhibits the highest gradients³⁴.

The experimental uncertainties for all types of measurements are discussed in Supplementary Note 5.

Numerical analysis. We start by fitting the total intensity for each wavevector (k_H, k_V) with a double Gaussian curve, which allows to find the energies of the two eigenstates (E_{\pm}) . Then, the intensities of the 6 polarisation components are obtained at the energies of the eigenstates by integration within the Gaussian width, and the components of the pseudospin calculated from these intensities. If the modes are almost degenerate in total intensity, with the energy difference falling below the inhomogeneous broadening, they can often still be distinguished by studying the spectra in polarisation components separately. This allows to resolve the branches for small energy differences. The pseudospin maps of the lower and upper eigenstates encoded in the angles θ and ϕ are then smoothed with a low-pass filter eliminating the noise. Finally, the components of the QGT are calculated from the pseudospin with Eqs. 4. The gradient is obtained by the Green-Gauss method with simple face averaging. Parallel computing is used to accelerate the treatment of 4.6×10^9 experimental data points. The final resolution of the QGT components is 1024×561 .

References

1. Berry, M. The quantum phase, five years after. In *Geometric phases in physics*, 7 (World Scientific, Singapore, 1989).
2. Berry, M. V. Quantal phase factors accompanying adiabatic changes. In *Proceedings of the Royal Society of London A: Mathematical, Physical and Engineering Sciences*, vol. 392, 45–57 (The Royal Society, 1984).
3. Hasan, M. Z. & Kane, C. L. Colloquium : Topological insulators. *Rev. Mod. Phys.* **82**, 3045–3067 (2010). URL <http://link.aps.org/doi/10.1103/RevModPhys.82.3045>.
4. Provost, J. & Vallee, G. Riemannian structure on manifolds of quantum states. *Communications in Mathematical Physics* **76**, 289–301 (1980).
5. Peotta, S. & Törmä, P. Superfluidity in topologically nontrivial flat bands. *Nature communications* **6**, 8944 (2015).
6. Gao, Y., Yang, S. A. & Niu, Q. Field induced positional shift of Bloch electrons and its dynamical implications. *Phys. Rev. Lett.* **112**, 166601 (2014). URL <https://link.aps.org/doi/10.1103/PhysRevLett.112.166601>.
7. Piéchon, F., Raoux, A., Fuchs, J.-N. & Montambaux, G. Geometric orbital susceptibility: Quantum metric without Berry curvature. *Phys. Rev. B* **94**, 134423 (2016). URL <https://link.aps.org/doi/10.1103/PhysRevB.94.134423>.

8. Srivastava, A. & Imamoglu, A. Signatures of Bloch-band geometry on excitons: Nonhydrogenic spectra in transition-metal dichalcogenides. *Phys. Rev. Lett.* **115**, 166802 (2015). URL <http://link.aps.org/doi/10.1103/PhysRevLett.115.166802>.
9. Bleu, O., Malpuech, G., Gao, Y. & Solnyshkov, D. D. Effective theory of nonadiabatic quantum evolution based on the quantum geometric tensor. *Phys. Rev. Lett.* **121**, 020401 (2018). URL <https://link.aps.org/doi/10.1103/PhysRevLett.121.020401>.
10. Kavokin, A., Baumberg, J. J., Malpuech, G. & Laussy, F. P. *Microcavities* (Oxford University Press, 2011).
11. Kavokin, A., Malpuech, G. & Glazov, M. Optical spin Hall effect. *Phys. Rev. Lett.* **95**, 136601 (2005). URL <http://link.aps.org/doi/10.1103/PhysRevLett.95.136601>.
12. Terças, H., Flayac, H., Solnyshkov, D. D. & Malpuech, G. Non-Abelian gauge fields in photonic cavities and photonic superfluids. *Phys. Rev. Lett.* **112**, 066402 (2014). URL <https://link.aps.org/doi/10.1103/PhysRevLett.112.066402>.
13. Haldane, F. D. M. & Raghu, S. Possible realization of directional optical waveguides in photonic crystals with broken time-reversal symmetry. *Phys. Rev. Lett.* **100**, 013904 (2008). URL <https://link.aps.org/doi/10.1103/PhysRevLett.100.013904>.
14. Lu, L., Joannopoulos, J. D. & Soljačić, M. Topological photonics. *Nature Photonics* **8**, 821–829 (2014).
15. Ozawa, T. *et al.* Topological photonics. *Rev. Mod. Phys.* **91**, 015006 (2019). URL <https://link.aps.org/doi/10.1103/RevModPhys.91.015006>.

16. Sundaram, G. & Niu, Q. Wave-packet dynamics in slowly perturbed crystals: Gradient corrections and berry-phase effects. *Phys. Rev. B* **59**, 14915–14925 (1999). URL <http://link.aps.org/doi/10.1103/PhysRevB.59.14915>.
17. Yang, Z. *et al.* Topological acoustics. *Phys. Rev. Lett.* **114**, 114301 (2015). URL <https://link.aps.org/doi/10.1103/PhysRevLett.114.114301>.
18. Cooper, N. R., Dalibard, J. & Spielman, I. B. Topological bands for ultracold atoms. *Rev. Mod. Phys.* **91**, 015005 (2019). URL <https://link.aps.org/doi/10.1103/RevModPhys.91.015005>.
19. Delplace, P., Marston, J. & Venaille, A. Topological origin of equatorial waves. *Science* **358**, 1075–1077 (2017).
20. Zanardi, P., Giorda, P. & Cozzini, M. Information-theoretic differential geometry of quantum phase transitions. *Phys. Rev. Lett.* **99**, 100603 (2007). URL <https://link.aps.org/doi/10.1103/PhysRevLett.99.100603>.
21. Liang, L., Peotta, S., Harju, A. & Törmä, P. Wave-packet dynamics of bogoliubov quasiparticles: Quantum metric effects. *Phys. Rev. B* **96**, 064511 (2017). URL <https://link.aps.org/doi/10.1103/PhysRevB.96.064511>.
22. Hauke, P., Lewenstein, M. & Eckardt, A. Tomography of band insulators from quench dynamics. *Phys. Rev. Lett.* **113**, 045303 (2014). URL <https://link.aps.org/doi/10.1103/PhysRevLett.113.045303>.

23. Lim, L.-K., Fuchs, J.-N. & Montambaux, G. Geometry of Bloch states probed by Stückelberg interferometry. *Phys. Rev. A* **92**, 063627 (2015). URL <https://link.aps.org/doi/10.1103/PhysRevA.92.063627>.
24. Fläschner, N. *et al.* Experimental reconstruction of the Berry curvature in a Floquet Bloch band. *Science* **352**, 1091–1094 (2016).
25. Wimmer, M., Price, H. M., Carusotto, I. & Peschel, U. Experimental measurement of the Berry curvature from anomalous transport. *Nature Physics* **13**, 545 (2017).
26. Yu, M. *et al.* Experimental measurement of the complete quantum geometry of a solid-state spin system. *arXiv:1811.12840* (2018).
27. Tan, X. *et al.* Experimental measurement of the quantum metric tensor and related topological phase transition with a superconducting qubit. *Phys. Rev. Lett.* **122**, 210401 (2019). URL <https://link.aps.org/doi/10.1103/PhysRevLett.122.210401>.
28. Bleu, O., Solnyshkov, D. D. & Malpuech, G. Measuring the quantum geometric tensor in two-dimensional photonic and exciton-polariton systems. *Phys. Rev. B* **97**, 195422 (2018). URL <https://link.aps.org/doi/10.1103/PhysRevB.97.195422>.
29. Richter, S. *et al.* Exceptional points in anisotropic planar microcavities. *Phys. Rev. A* **95**, 023836 (2017). URL <https://link.aps.org/doi/10.1103/PhysRevA.95.023836>.

30. Nalitov, A. V., Solnyshkov, D. D. & Malpuech, G. Polariton \mathbb{Z} topological insulator. *Phys. Rev. Lett.* **114**, 116401 (2015). URL <https://link.aps.org/doi/10.1103/PhysRevLett.114.116401>.
31. Klemmt, S. *et al.* Exciton-polariton topological insulator. *Nature* **562**, 552 (2018).
32. St-Jean, P. *et al.* Lasing in topological edge states of a one-dimensional lattice. *Nature Photonics* **11**, 651 (2017).
33. Bleu, O., Malpuech, G. & Solnyshkov, D. D. Robust quantum valley hall effect for vortices in an interacting bosonic quantum fluid. *Nature Comm* **9**, 3991 (2018). URL <https://www.nature.com/articles/s41467-018-06520-7>.
34. Steger, M., Gautham, C., Snoke, D. W., Pfeiffer, L. & West, K. Slow reflection and two-photon generation of microcavity exciton-polaritons. *Optica* **2**, 1–5 (2015). URL <http://www.osapublishing.org/optica/abstract.cfm?URI=optica-2-1-1>.
35. Ballarini, D. *et al.* Macroscopic two-dimensional polariton condensates. *Phys. Rev. Lett.* **118**, 215301 (2017). URL <https://link.aps.org/doi/10.1103/PhysRevLett.118.215301>.
36. Armitage, A. *et al.* Exciton polaritons in semiconductor quantum microcavities in a high magnetic field. *Phys. Rev. B* **55**, 16395–16403 (1997). URL <https://link.aps.org/doi/10.1103/PhysRevB.55.16395>.

37. Rahimi-Iman, A. *et al.* Zeeman splitting and diamagnetic shift of spatially confined quantum-well exciton polaritons in an external magnetic field. *Phys. Rev. B* **84**, 165325 (2011). URL <https://link.aps.org/doi/10.1103/PhysRevB.84.165325>.

Acknowledgements We thank David Colas for critical reading of the manuscript. This work was supported by the ERC project "ElecOpteR" (grant N. 780757). We acknowledge the support of the project "Quantum Fluids of Light" (ANR-16-CE30-0021), of the ANR Labex Ganex (ANR-11-LABX-0014), and of the ANR program "Investissements d'Avenir" through the IDEX-ISITE initiative 16-IDEX-0001 (CAP 20-25). D.D.S. acknowledges the support of IUF (Institut Universitaire de France).

Author contributions A.G., L.D., and D.B. designed the setup. A.G. realised the experiments with the help of V.A., M.D.G., and G.L. D.S. supervised the experimental part. K.W. and L.N.P. fabricated the sample. O.B., D.D.S., and G.M. performed the treatment of the experimental data. O.B. performed analytical calculations. G.M. and O.B. wrote the manuscript with inputs from all authors.

Competing Interests The authors declare that they have no competing financial interests.

Correspondence Correspondence should be addressed to G. Malpuech (E-mail: guillaume.malpuech@uca.fr) and D. Sanvitto (E-mail: daniele.sanvitto@nano.cnr.it).

Supplementary Notes for the Manuscript entitled:
"Direct measurement of the quantum geometric tensor
and of the anomalous Hall drift in a two-dimensional
continuous medium"

A. Gianfrate¹, O. Bleu^{2*}, L. Dominici¹, V. Ardizzone¹, M. De Giorgi¹,
D. Ballarini¹, G. Lerario¹, K. West³, L. N. Pfeiffer³, D. D. Solnyshkov²,
D. Sanvitto¹, G. Malpuech²

1. CNR NANOTEC, Istituto di Nanotecnologia, via Monteroni, 73100 Lecce, Italy.
2. Institut Pascal, PHOTON-N2, Université Clermont Auvergne, CNRS, SIGMA Clermont, F-63000 Clermont-Ferrand, France.
3. PRISM, Princeton Institute for the Science and Technology of Materials, Princeton University, Princeton, New Jersey 08540, USA

October 2, 2019

Abstract

This supplementary material is composed of five notes. The first note presents analytical formula used to compute the quantum metric and Berry curvature and which are taken from [1]. In the second note, we present the raw Photoluminescence data and the deconvolution procedure used to obtain the experimental data presented in the main manuscript. The third note discusses the measurements of the anomalous Hall drift. The fourth note concerns the associated non-adiabaticity and quantum metric effects. Finally, the fifth note presents the estimates of the experimental uncertainties.

The Supplementary Figures present the raw PL data (Suppl. Figs. 1-3), extracted experimental images of the Berry curvature and the quantum metric of the upper polarisation mode (Suppl. Fig. 4), additional trajectories and profiles for the anomalous Hall drift (Suppl. Fig. 5) and, finally, polariton dispersion measurement on a large scale (Suppl. Fig. 6) evidencing exciton-photon anticrossing.

*These authors contributed equally: A. Gianfrate, O. Bleu

Supplementary Note 1. Analytical expressions for quantum metric and Berry curvature

For a given band, the elements of the quantum geometric tensor can be defined as:

$$T_{ij}^{(n)} = \sum_{m \neq n} \frac{\langle \psi_m | \partial_{k_i} H_k | \psi_n \rangle \langle \psi_n | \partial_{k_j} H_k | \psi_m \rangle}{(E_m - E_n)^2} \quad (1)$$

where H_k is the k -dependent Hamiltonian, $|\psi_n\rangle$ and E_n the corresponding eigenstates and eigenenergies (n is the band index). The quantum metric tensor and the Berry curvature tensor are obtained from real symmetric and the imaginary antisymmetric part of (1):

$$g_{ij}^{(n)} = \text{Re} [T_{ij}^{(n)}], \quad \Omega_{ij}^{(n)} = -2 \text{Im} [T_{ij}^{(n)}] = i (T_{ij}^{(n)} - T_{ji}^{(n)}) \quad (2)$$

For a two-band system, these definitions imply that the metric elements of each band are equal $g_{ij}^{(1)} = g_{ij}^{(2)}$ whereas the Berry curvature ones are opposite. In three dimensional space, the Berry curvature can be represented as a pseudo-vector $\mathbf{B}^{(n)} = (\Omega_{23}^{(n)}, \Omega_{31}^{(n)}, \Omega_{12}^{(n)})^T$. Since the system under study is a planar structure, the only non-zero component of $\mathbf{B}^{(n)}$ is out of the plane, along the z-direction.

Starting with the effective Hamiltonian presented in the main text, one can obtain the analytical expressions of the quantum geometric tensor elements:

$$\begin{aligned} g_{HH} &= \frac{\beta^2 \left(k_H^2 (\alpha - k^2 \beta)^2 + k^2 \Delta_z^2 \right)}{(\alpha^2 + 2(k_V^2 - k_H^2) \alpha \beta + k^4 \beta^2 + \Delta_z^2)^2} \\ g_{VV} &= \frac{\beta^2 \left(k_V^2 (\alpha + k^2 \beta)^2 + k^2 \Delta_z^2 \right)}{(\alpha^2 + 2(k_V^2 - k_H^2) \alpha \beta + k^4 \beta^2 + \Delta_z^2)^2} \\ g_{HV} &= \frac{\beta^2 k_H k_V (\alpha^2 - k^4 \beta^2)}{(\alpha^2 + 2(k_V^2 - k_H^2) \alpha \beta + k^4 \beta^2 + \Delta_z^2)^2} \\ B_z &= \frac{2\beta^2 k^2 \Delta_z}{(\alpha^2 + 2(k_V^2 - k_H^2) \alpha \beta + k^4 \beta^2 + \Delta_z^2)^{3/2}} \end{aligned} \quad (3)$$

In the figure 4 of the main text, we use the above expressions for a direct comparison with the experimental extraction, the value of α , β , and Δ_z being extracted from the experimental data.

Supplementary Note 2. Raw Photoluminescence data and its treatment

The Supplementary Figure 1 shows the raw PL spectra versus k_H measured at 9 T: (a) - total intensity, (b) - left-circular, (c) - right-circular. One can see that the lines are well resolved, with the splitting exceeding their broadening (of all origins) everywhere. They show a substantial circular polarisation degree near $k = 0$.

The Supplementary Figure 2 shows the photoluminescence intensity measured again at 9 T in the four linear polarisation projections: horizontal (a), vertical (b), diagonal (c), and anti-diagonal (d), versus the wave vector k at a given energy (4.5 meV above $k = 0$), where the mode structure is governed by the TE-TM splitting. One clearly sees the presence of two interleaved circles. For each direction in the reciprocal space, the polarisations of the inner and outer circles are orthogonal. The polarisation patterns, presented in the main text (Fig. 2(b,c), Fig. 3(b,c,d)) are extracted from these types of measurements.

One should note, however, that the energy difference between modes is quite smaller at 0 T, where the modes are even crossing at two points in reciprocal space. The Supplementary Figure 3(a) shows the total intensity taken at 0 T along k_H respectively. One can see that the mode splitting close to $k = 0$ is not straightforwardly resolved since the splittings are comparable with the linewidth. This is imposing the use of a standard deconvolution procedure to extract the two modes energy and polarisations for each wave vector. We ultimately used this procedure to treat all the sets of data.

The measured k-space polarisation patterns of the main text, even if very clear, show some short scale fluctuations due to the experimental setup. These fluctuations would induce errors in the computation of the quantum geometric tensor elements, because their calculation requires taking derivatives. We therefore use a low-pass spectral filtering procedure. The procedure is based on the 2D Fourier transform of the k-space polarisation, removal of the fluctuations, and inverse Fourier transform. This allows to get a pseudo spin texture cleaned of experimental noise (Fig. 2(d,e), Fig. 3(e)) and then to compute the different elements of the quantum geometric tensor shown in Fig. 2(f) and Fig. 4(a-d).

In order to compensate the inevitable angles between the axes of the CCD camera (x,y), the polarizer axes (H,V), and the crystallographic axes of the sample, we have rotated the in-plane components of the Stokes vector for all measured points, and the points themselves. This allows to use a single set of axes throughout the manuscript. The Supplementary Figure 2 shows an example of non-rotated data.

Supplementary Note 3. Anomalous Hall effect

In this supplementary note, we discuss the anomalous Hall effect and the details of its measurement. First, we provide a simple analytical estimate based on the monopolar nature of the gauge field arising in the reciprocal space because of the interplay of the constant XY field with the k -dependent TE-TM effective field. Then, we discuss the treatment of the experimental data and the different types of corresponding numerical simulations.

A monopolar in-plane effective field combined with a Zeeman splitting is equivalent to the well-studied configuration of the 2D Dirac Hamiltonian, which describes not only relativistic electrons and positrons in 2D, but also many analog systems, in particular, the wide class of 2D materials (graphene, transitional metal dichalcogenides). The maximal anomalous Hall drift due to the Berry curvature in such systems can be simply estimated as the double of the Compton electron wavelength, which is the combination of parameters of the Dirac equation with the dimensions of length:

$$\lambda_{Compt} = \frac{\hbar}{mc} \quad (4)$$

The parameters m and c in our case should be chosen to describe the dispersion at the anticrossing point $k_0 = \sqrt{\alpha/\beta}$: the slope of the dispersion c is given by $\hbar c = \sqrt{\beta\alpha/2}$, and the mass corresponds to the splitting of the branches $mc^2 = \Delta_z$, which gives the estimation for the maximal anomalous Hall drift:

$$\Delta Y_{AHE} = \frac{\sqrt{2\beta\alpha}}{\Delta_z} \quad (5)$$

This expression can be compared with the anomalous Hall drift without the in-plane field found in [2]:

$$\Delta Y_0 = \frac{\sqrt{\beta}\Gamma^2(3/4)}{\sqrt{\Delta_z}\sqrt{\pi}} \quad (6)$$

An important difference is that the dependence on the Zeeman splitting changes: it is stronger in presence of the in-plane field α , because the Berry curvature becomes completely concentrated in the anticrossing points, and not distributed along a ring in the reciprocal space.

A stronger sensitivity to the Zeeman splitting allows to increase the anomalous Hall drift by shifting towards more negative detunings. With the parameters extracted from the experimental dispersion in the main text corrected by the detuning $\delta = -10$ meV we obtain $\Delta Y_{AHE} \approx 0.7 \mu\text{m}$.

The experiment on the polariton anomalous Hall drift is discussed in the main text and shown in Fig. 5(a). Here, we discuss the details of the treatment of the experimental data used to obtain the trajectories shown in Fig. 5(b). We start with the spatial distribution of intensity $I(x, y)$ for two configurations (+9 and -9 T). First, we determine the average propagation direction (black arrow in Fig. 5(a)), which is chosen as the horizontal (X) axis. Then, for each point along X, we calculate the center of mass position of the wave packet in the transverse direction (Y). The position of the center of mass along the Y coordinate for a given value of x is defined as:

$$\langle Y(x) \rangle = \frac{\int y I(x, y) dy}{\int I(x, y) dy} \quad (7)$$

We then use a sliding average procedure to obtain the smoothed trajectories shown by points in Fig. 5(b) and also in Supplementary Figure 5(a). The error bars are given by the average value of the standard deviation within each group of experimental points represented by a single point of the smoothed trajectory.

In order to demonstrate that the anomalous Hall drift is clearly present without any smoothing, we show the difference between the center of mass positions along the Y axis in the two configurations (+9 and -9T) $\Delta Y(X)$ for all points. A linear least-mean-square fit allows to

extract an average "double" drift of $7 \pm 1 \text{ nm}/\mu\text{m}$, clearly different from zero. We note that this value is the double of the drift of a single wavepacket in a single experiment, because it is a difference between two opposite drifts.

The configuration of our experiment is particularly favourable for the observation of the anomalous Hall drift thanks to the presence of a saddle-type component in the potential created for polaritons by the variation of the cavity thickness. To take into account the precise properties of this potential $U(x, y)$, we have scanned the energy of the lower polariton branch at $k = 0$ in a wide region ($660 \mu\text{m} \times 580 \mu\text{m}$) and determined its first derivatives (the gradient) and the second derivatives (variations of the gradient). We have obtained a gradient $\partial U/\partial x = -5.8 \pm 0.2 \text{ meV}/\text{mm}$, and a second derivative $\partial^2 U/\partial y^2 = -(2.0 \pm 0.2) \times 10^{-2} \mu\text{eV}/\mu\text{m}^2$ (in the direction transverse to the gradient). This second derivative acts like a magnifying glass, amplifying the differences between the trajectories in the +9 T and -9 T configurations.

In the main text, we present the results of the simulations of the wave packet propagation with the semiclassical equation, where this potential is fully taken into account via \mathbf{F} . The Supplementary Figure 5(a) presents, in addition, the results of the full numerical simulation based on a 2D Schrödinger equation (which is equivalent to the Maxwell's equations for the transverse beam profile in the paraxial approximation):

$$i\hbar \frac{\partial \psi_{\pm}}{\partial t} = -\frac{\hbar^2}{2m} \Delta \psi_{\pm} - \frac{i\hbar}{2\tau} \psi_{\pm} \pm \Delta_z \psi_{\pm} \quad (8)$$

$$+ \beta \left(\frac{\partial}{\partial x} \mp i \frac{\partial}{\partial y} \right)^2 \psi_{\mp} + \alpha \psi_{\mp} + U \psi_{\pm} + \hat{P}$$

where P is the pump, $\tau = 100 \text{ ps}$ is the polariton lifetime. The corresponding trajectories are plotted with solid lines. They confirm the validity of the results obtained in the semiclassical approximation with the same potential (dash-dotted lines).

In order to understand the relative contribution of the magnifying effect of the saddle-type potential we also plot the semiclassical trajectories with a constant gradient (dashed lines). The increase of the divergence of the two trajectories is substantial, but even without the saddle-type potential the drift is non-negligible.

The same three results are also plotted in Fig. 5(b), showing the difference between the two configurations (+9 T and -9 T). Both the full Schrödinger simulation (blue) and the semiclassical equation with saddle-type potential (cyan) allow to reproduce correctly the experimental "double" drift of $7 \pm 1 \text{ nm}/\mu\text{m}$, whereas the pure semiclassical calculation (red solid line) shows a smaller (but also quite substantial) drift.

The uncertainties of these (and other) experimental measurements are discussed in Supplementary Note 5.

As an illustration, we show the transverse profiles of the polariton flow in Fig. 5(c). Fitting these profiles with a Gaussian function allows to extract the parameters of the wavepacket, such as its width and its position. At $X = 50 \mu\text{m}$, the fit with $R^2 = 0.98$ gives a FWHM of $36 \pm 1 \mu\text{m}$ and $34 \pm 1 \mu\text{m}$ at +9 T and -9 T, respectively. The transverse position y_0 at $X = 50 \mu\text{m}$ is $0 \pm 0.2 \mu\text{m}$ for both +9 T and -9 T. During the propagation, the two wave packets shift laterally. The final profile at $X = 350 \mu\text{m}$ gives the transverse position of $y_0 = +1.7 \pm 0.2 \mu\text{m}$ for +9 T and $y_0 = -1.0 \pm 0.2 \mu\text{m}$, which gives a difference of $2.7 \pm 0.4 \mu\text{m}$. This is compatible with a "double" drift of $7 \pm 1 \text{ nm}/\mu\text{m}$ found above.

We stress, however, that the direct treatment of these profiles does not allow to extract the anomalous Hall drift with a high confidence level for several reasons. First, the profile does not have to be a Gaussian (because of the spin conversion and disorder), and in a general case it is not. It is the *centre of mass* of the wavepacket that has to obey the semiclassical equation of motion, and not the center of a Gaussian fit. Second, the transverse position exhibits large fluctuations (as seen in panel (b)), and a significant averaging along the propagation direction is required to get meaningful values. This is why the profiles shown in Fig. 5(c) should really be used rather as an illustration.

Supplementary Note 4. The effects of the quantum metric on the anomalous Hall drift

The semiclassical equation for the trajectory of the wave packet describes only the adiabatic part of the wave function, that is, the fraction which is aligned with the effective field. The non-adiabatic fraction appears both because of the conditions of the excitation and during the evolution of the wave packet because of its finite velocity in the reciprocal space. We have performed additional experiment to emphasize the role of the metric by creating a substantial initial non-adiabaticity controlled by the choice of the laser polarisation.

We begin by writing a general superposition $|\psi\rangle = f_0 |\psi_0\rangle + f_1 |\psi_1\rangle$, where $|\psi_0\rangle$ corresponds to the lower band and $|\psi_1\rangle$ corresponds to the upper band. The fractions of the bands can be found as

$$|f_0|^2 = \int \frac{e^{-\frac{k^2}{2\sigma^2}}}{\sqrt{2\pi\sigma^2}} |\langle\psi_l|\psi_0(\mathbf{k})\rangle|^2 d^2k \quad (9)$$

$$|f_1|^2 = \int \frac{e^{-\frac{k^2}{2\sigma^2}}}{\sqrt{2\pi\sigma^2}} |\langle\psi_l|\psi_1(\mathbf{k})\rangle|^2 d^2k \quad (10)$$

where $|\psi_l\rangle$ describes the polarization state of the laser (circular polarization). The overlap integrals are determined by the quantum metric of the reciprocal space:

$$|\langle\psi_l|\psi_1\rangle|^2 = 1 - \left(\int_{|\psi_0\rangle}^{|\psi_l\rangle} \sqrt{\sum_{ij} g_{ij} \frac{dk^i}{dt} \frac{dk^j}{dt}} dt \right)^2 \quad (11)$$

where the integral is taken along the shortest distance path between the two points. Using the orthogonality of the states $|\psi_0\rangle$ and $|\psi_1\rangle$ we can finally write

$$|f_1|^2 = \int \frac{e^{-\frac{k^2}{2\sigma^2}}}{\sqrt{2\pi\sigma^2}} \left(\int_{|\psi_0(\mathbf{k})\rangle}^{|\psi_l\rangle} \sqrt{\sum_{ij} g_{ij} \frac{dk^i}{dt} \frac{dk^j}{dt}} dt \right)^2 d^2k \quad (12)$$

In the particular experimental conditions, when the laser is circular polarized, its spinor state corresponds to the wavefunction at the anticrossing point: $|\psi_l\rangle = |\psi_0(k_0)\rangle$, whereas the excitation wave vector determines the lower bound of the integral $|\psi_0(0)\rangle$. Assuming that the wave packet is sufficiently small in the reciprocal space, that is, $\sigma_k \ll k_0$, we can estimate the non-adiabatic fraction as:

$$|f_1|^2 \approx \left(\int_{|\psi_0(0)\rangle}^{|\psi_0(k_0)\rangle} \sqrt{\sum_{ij} g_{ij} \frac{dk^i}{dt} \frac{dk^j}{dt}} dt \right)^2 \quad (13)$$

This expression allows us to link the oscillations observed in the cross-polarization (corresponding to the non-adiabatic fraction) in the experimental measurement of the anomalous Hall drift with the quantum metric. Indeed, the non-adiabatic fraction determines the angle η between the effective field and the pseudospin of the state: $|f_1|^2 = 1 - \cos^2 \eta = \sin^2 \eta$, which for small η gives simply $|f_1|^2 \approx \eta^2$. In the regime of dominant initial non-adiabaticity, this angle (together with the non-adiabatic fraction) remains constant during the propagation of the wave packet and the associated evolution of the effective field. For long propagation distances, the effective field is almost in the plane, and the polar angle of the pseudospin, during the

precession of the latter about the effective field, oscillates between $\pi/2 + \eta$ and $\pi/2 - \eta$, which means that the intensity of the cross-polarized component varies between $\sin^2((\pi/2 + \eta)/2)$ and $\sin^2((\pi/2 - \eta)/2)$ or approximately between $1/2 - \eta/2$ and $1/2 + \eta/2$. The contrast of these oscillations gives

$$C = \frac{I_{max} - I_{min}}{I_{max} + I_{min}} \approx \eta \quad (14)$$

Therefore, measuring the contrast at later times gives directly the deviation angle and the associated non-adiabatic fraction $|f_1|^2 = C^2$ linked with the metric. The quantum distance that we estimate from the oscillations in the experimentally measured cross polarization is 0.16 ± 0.02 , while the expression (13) gives 0.18 ± 0.03 .

Supplementary Note 5. Estimation of the measurement uncertainty

In this supplementary note, we discuss the uncertainty of our experimental measurements. Different measured quantities are discussed in corresponding subsections. For all fitting procedures in all sections we use the non-linear least squares procedure with the Levenberg-Marquardt error minimization algorithm, with the confidence interval for parameter values obtained from the variance-covariance matrix using the asymptotic symmetry method.

Pseudospin distribution

Each point of the measured pseudospin distributions shown in Figs. 2 and 3 of the main text is subject to experimental uncertainty. For each point, the PL curve similar to the one shown in Supplementary Figure 3 is fitted with a Gaussian function for each polarization. As an example, for a typical point in the highly-circular polarized region, the amplitude of the Gaussian for a given polarization is determined with 1.2% precision, and its width with 1.5% precision. These confidence intervals obtained for the amplitude and the width of each of the Gaussian functions from the Levenberg-Marquardt algorithm at 95% confidence level allow to determine the final relative precision on the pseudospin components (by comparing the maximal and the minimal possible value of the component), which is about 10% (or smaller, depending on the local polarization degree). The corresponding deviations of the pseudospin from the local average value are clearly visible in Figs. 2 and 3 of the main text. However, they are mostly short-scale and/or uncorrelated, which allows to suppress them by using filtering for the calculation of the Berry curvature and the quantum metric.

Berry curvature

The short-scale fluctuations linked with the uncertainty of the pseudospin extraction are eliminated before the calculation of the Berry curvature by using low-pass spatial filtering. However, this procedure cannot remove efficiently the large-scale fluctuations of the pseudospin, and at the same time it smooths out the real variations of the pseudospin due to the interplay of the SOC with the Zeeman splitting. In order to estimate the uncertainty introduced by filtering, we compare the filtered pseudospin distributions with the original ones. In particular, we compare the local average pseudospin value with the result of the filtering. This comparison reveals that the deviations after the filtering procedure are of the order of 5%. The advantage of filtering is that these deviations are all large-scale, and are therefore not amplified by taking the derivatives. In the worst case, the product of two derivatives appearing in the Berry curvature (Eq. (4) of the main text) gives a doubled relative error. The final estimate of the precision on the determination of the points in Fig. 4 of the main text is therefore of the order of 10%.

Parameters of the effective Hamiltonian

The parameters of the effective Hamiltonian are determined from the experimentally measured dispersions by fitting them with the analytical expression for the dispersion obtained from the effective Hamiltonian (1) of the main text. confidence interval in its turn determines the relative uncertainty values given in the Methods section.

Center of mass measurement

In the experiment, the intensity of emission is measured on a finite-step grid: $I(x_n, y_n)$. The wave packet is accelerated by a gradient along the X direction and is expected to exhibit a transverse anomalous Hall drift in the Y direction. We need therefore to analyze the position of the center of mass along the Y direction with the highest possible precision. The step (pixel size) $h = y_n - y_{n-1}$ is $1.29 \mu\text{m}$. The position of the center of mass along the Y coordinate for a given value of x is defined as the mathematical expectation of the Y coordinate, if the intensity distribution is considered as a probability density (as already discussed in Supplementary Note 3):

$$\langle Y(x) \rangle = \frac{\int y I(x, y) dy}{\int I(x, y) dy} \quad (15)$$

In practice, the continuous integral in (15) is replaced by a Riemann sum with the step h . In order to maximize the precision, we use the midpoint rule:

$$\int f(y) dy \approx S = h \sum_1^n f(y_i^*) \quad (16)$$

where $y_i^* = (y_{i+1} - y_i)/2$. The error of this method (which is entirely due to the finite step size) is estimated by

$$\left| \int_a^b f(y) dy - S \right| \leq \frac{(b-a)^3 \max f''(y)}{24n^2} \quad (17)$$

In order to evaluate this error, we first find the maximal value of the second derivative of the intensity distribution, which we first assume to be a Gaussian (valid in most of the moments of time during the wave packet evolution):

$$\frac{I(x_0, y)}{\int I(x_0, y) dy} = \frac{1}{\sigma\sqrt{2\pi}} \exp\left(-\frac{y^2}{2\sigma^2}\right) = f(y) \quad (18)$$

The second derivative reads

$$f''(y) = \frac{(y^3 - 3\sigma^2 y) e^{-y^2/2\sigma^2}}{\sigma^5 \sqrt{2\pi}} \quad (19)$$

Its maximal value is achieved for $y = \sigma\sqrt{3 - \sqrt{6}}$. This maximal value is given by

$$\max f''(y) = \frac{\sqrt{\frac{9-3\sqrt{6}}{\pi}} e^{-\frac{3}{2} + \sqrt{\frac{3}{2}}}}{\sigma^2} \approx \frac{0.55}{\sigma^2} \quad (20)$$

Another important parameter is the integration interval $b - a$, determined by the noise. In our case, $b - a \approx 6\sigma$. Finally, the number of steps $n = (b - a)/h = 6\sigma/h$. This allows to write the final expression:

$$\Delta Y = \frac{(6\sigma)^3 0.55}{24\sigma^2 (6\sigma/h)^2} \approx \frac{h^2}{8\sigma} \quad (21)$$

This analysis clearly shows that the error on the center of mass position for large wave packets can be much smaller than the step size. In our case, $h = 1.29 \mu\text{m}$, $\sigma \sim 10 \mu\text{m}$, which allows to determine the wave packet center of mass position with a precision up to $0.02 \mu\text{m}$.

For a multi-peak distribution, the maximal value of the second derivative is determined by the narrowest peak: $\max f''(y) \approx 0.6/\sigma_{min}^2$. One has to use the expression (17), which writes:

$$\Delta Y \approx \frac{Lh^2}{40\sigma^2} \quad (22)$$

where L is the multi-peak region over which the integration is carried out. Taking the typical values of $L = 50 \mu\text{m}$ and $\sigma = 5 \mu\text{m}$ (for a particularly narrow peak), we obtain an error of $\Delta Y = 0.09 \mu\text{m}$. This precision is still sufficient for the measurement of the deviation caused by the anomalous Hall effect.

We note that the uncertainty ΔY from this Note should not be confused with the difference between the center of mass trajectories $\Delta Y(X)$ from the Supplementary Note 3 and Supplementary Figure 5.

The above analysis applies only to the "quantization noise", linked with the finite spatial step of the measurements h . We now estimate the contribution of the intensity noise by using the linearity of the expression for the center of mass (15). Indeed, if the center of mass position of the pure signal is given by Y_s , the measured center of mass position can be found as

$$Y_m = Y_s I_s + Y_n I_n \quad (23)$$

where I_s is the signal intensity, I_n is the noise intensity and Y_n is the noise center of mass position. The experimental detector noise is well described as a positive constant plus a spatially uniform noise with a Gaussian amplitude distribution. The average integrated noise intensity is therefore given by the standard deviation of its amplitude times L , while the error on its center of mass position is given by the standard deviation of the uniform distribution. The final error on the measured center of mass position is given by:

$$\Delta Y = \frac{L I_n}{2\sqrt{3} I_s} \quad (24)$$

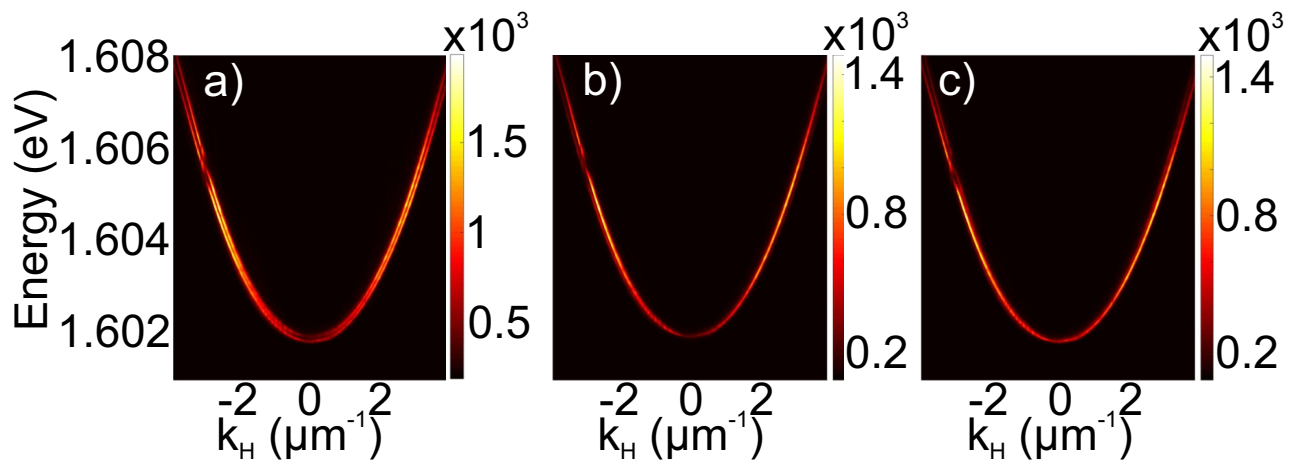
which gives for experimental values of $I_n/I_s \approx 0.01$ (integrated within $L = 50 \mu\text{m}$) $\Delta Y = 0.15 \mu\text{m}$.

The total error on the center of mass position, taking into account the finite step size and the detector noise, is of the order of $0.24 \mu\text{m}$. This is comparable with the expected amplitude of the effect for large excitonic fractions, but smaller than the expected anomalous Hall drift for smaller excitonic and larger photonic fractions. The observed drift is moreover amplified by the saddle-type potential present in the system, which makes our measurement sufficiently reliable.

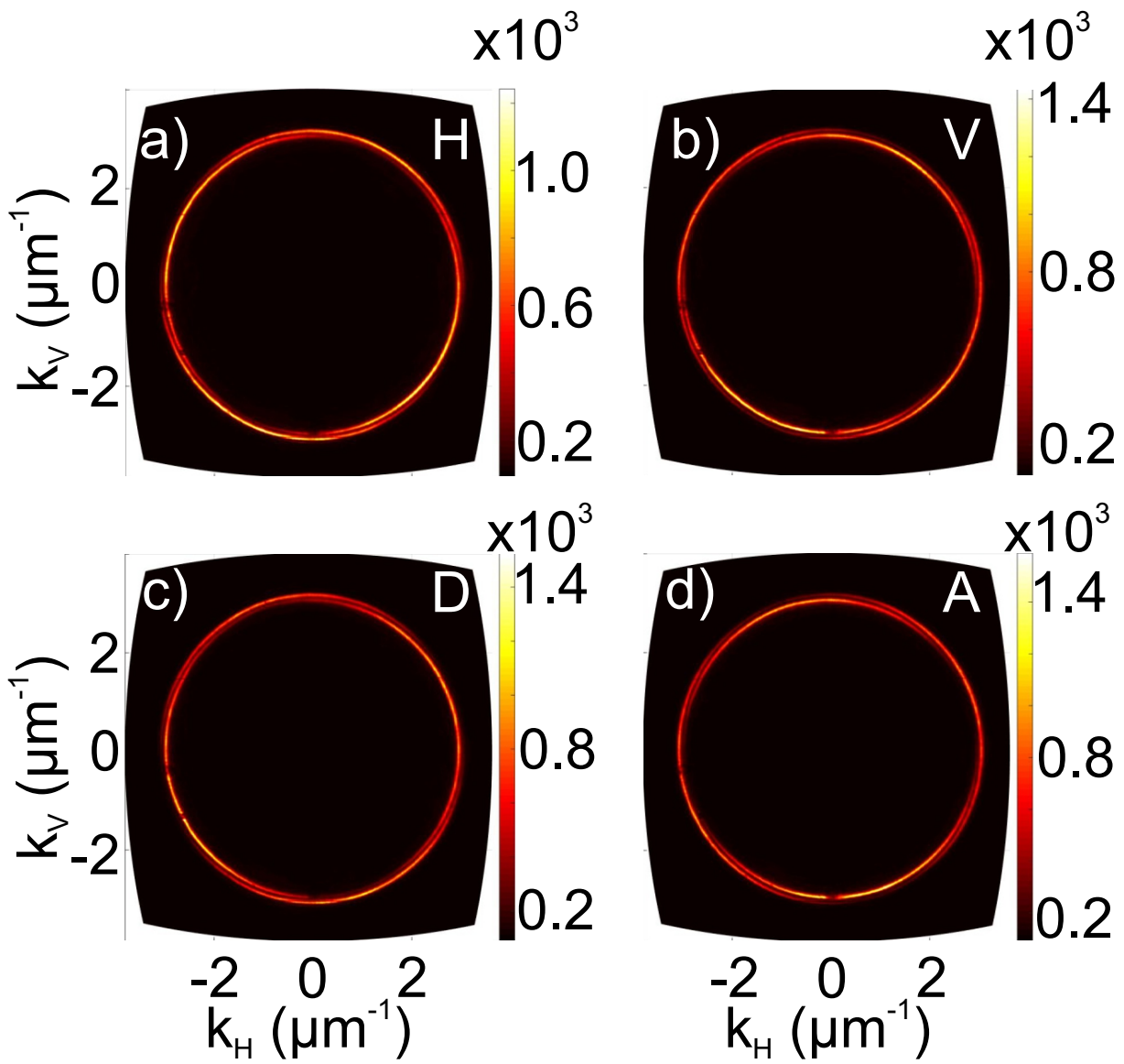
Supplementary References

- [1] Bleu, O., Solnyshkov, D. D. & Malpuech, G. Measuring the quantum geometric tensor in two-dimensional photonic and exciton-polariton systems. *Phys. Rev. B* **97**, 195422 (2018). URL <https://link.aps.org/doi/10.1103/PhysRevB.97.195422>.
- [2] Bleu, O., Malpuech, G., Gao, Y. & Solnyshkov, D. D. Effective theory of nonadiabatic quantum evolution based on the quantum geometric tensor. *Phys. Rev. Lett.* **121**, 020401 (2018). URL <https://link.aps.org/doi/10.1103/PhysRevLett.121.020401>.

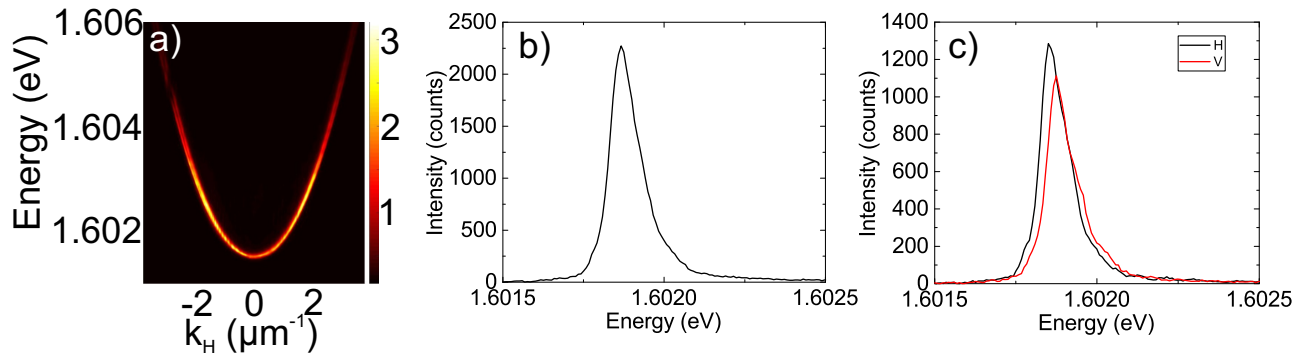
Supplementary figures



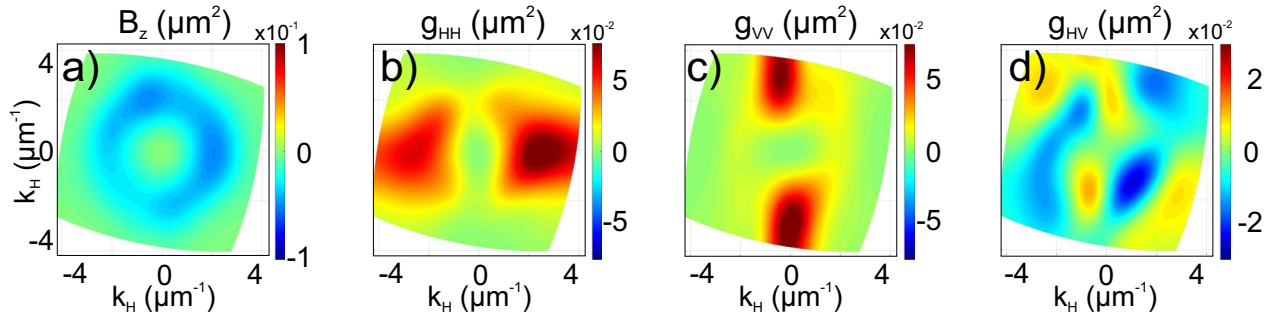
Supplementary Figure 1: Measured photoluminescence intensity as a function of energy and wave vector at 9 Tesla: a) total, b) left-circular, c) right-circular.



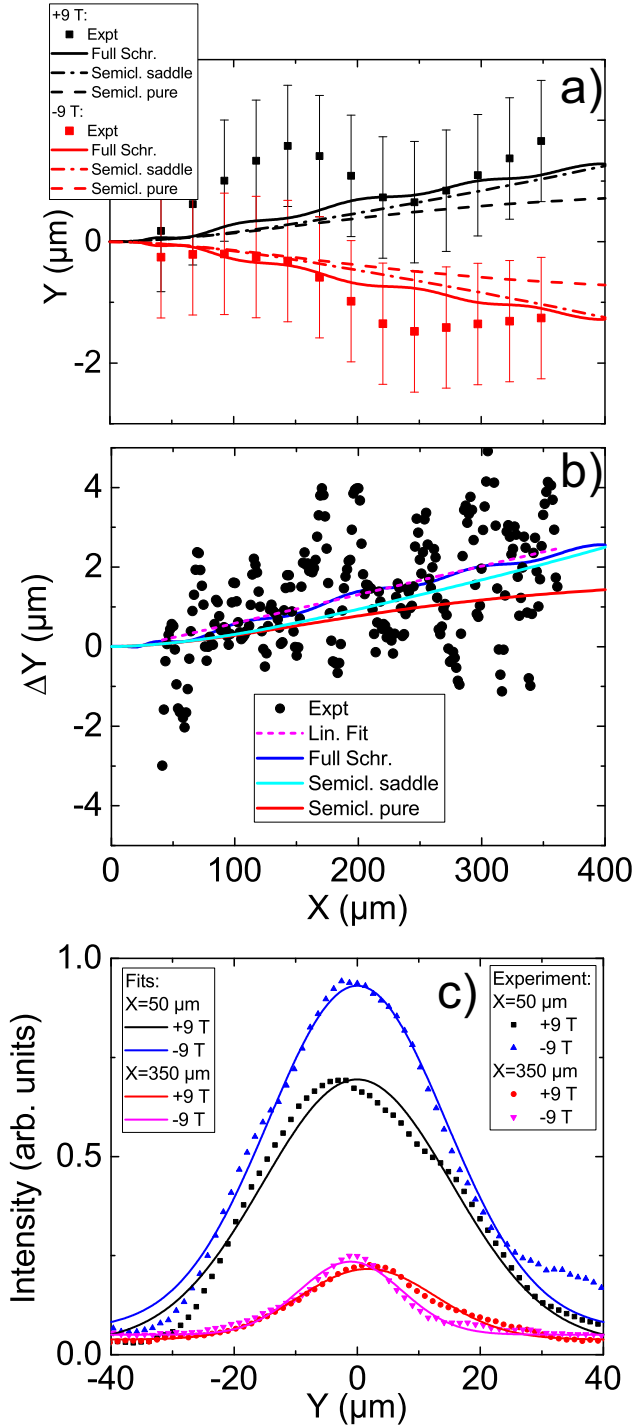
Supplementary Figure 2: Measured photoluminescence intensity as a function of in-plane wave vector, 4.5 meV above the ground state energy and under 9 Tesla: a) horizontal, b) vertical, c) diagonal, d) anti-diagonal.



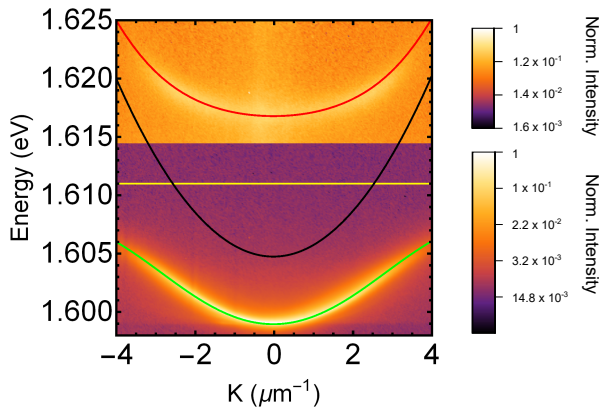
Supplementary Figure 3: Measured photoluminescence intensity at 0 Tesla: a) total intensity as a function of wave vector and energy, b) total intensity as a function of energy only, for wave vector $k_H = 1.46 \mu\text{m}^{-1}$; c) intensities in H and V polarisations for the same wave vector.



Supplementary Figure 4: Berry curvature and quantum metric for the upper branch, measured at 9 T. k -space distribution of quantum geometric tensor elements: (a) Berry curvature B_z , (b) g_{HH} , (c) g_{VV} , (d) g_{HV} , extracted using Eq. (4) of the main text.



Supplementary Figure 5: Wavepacket center of mass trajectories in the anomalous Hall effect. a) Trajectories in the +9 and -9 T configurations: experiment (points with error bars), full Schrödinger simulation (solid lines), semiclassical equation with saddle-type potential (dash-dotted lines), semiclassical equation with a constant gradient (dashed lines). b) Difference between the +9 and -9 T configurations: experiment (points), linear fit (red dashed line), full Schrödinger simulation (blue line), semiclassical equation with saddle-type potential (cyan line), semiclassical equation with a constant gradient (red solid line). c) Transverse profiles of the polariton flow at $X = 50 \mu\text{m}$ and $X = 350 \mu\text{m}$ at $\pm 9 \text{ T}$ (points) with Gaussian fits (solid lines), giving the initial positions $y_0 = 0.0 \pm 0.2 \mu\text{m}$ at $X = 50 \mu\text{m}$ and the final positions $y_0(+9 \text{ T}) = 1.7 \pm 0.2 \mu\text{m}$ vs $y_0(-9 \text{ T}) = -1.0 \pm 0.2 \mu\text{m}$.



Supplementary Figure 6: Energy dispersion of the polariton emission under cw non-resonant excitation (1.689 eV) at 0 T. The strong coupling between the exciton transition (yellow line) and the photon mode (black line) leads to the generation of the upper and lower polariton modes. The intensity map is plotted in log scale in order to highlight the anticrossing behaviour. Two different scales are used for the lower and upper part of the figure in order to be able to better visualise the modes. The green and red lines correspond to the theoretical upper and lower polariton dispersions obtained considering a two coupled oscillators model. The Rabi energy splitting is 16.2 meV.